New Journal of Physics
The open access journal at the forefront of physics

Deutsche Physikalische Gesellschaft DPG IOP Institute of Physics

PAPER • OPEN ACCESS

Atomic source selection in space-borne gravitational wave detection

To cite this article: S Loriani *et al* 2019 *New J. Phys.* **21** 063030

New Journal of Physics
The open access journal at the forefront of physics

Deutsche Physikalische Gesellschaft DPG
IOP Institute of Physics

Published in partnership with: Deutsche Physikalische Gesellschaft and the Institute of Physics

OPEN ACCESS

RECEIVED
28 December 2018

REVISED
5 April 2019

ACCEPTED FOR PUBLICATION
20 May 2019

PUBLISHED
21 June 2019

PAPER

Atomic source selection in space-borne gravitational wave detection

S Loriani[1], D Schlippert[1], C Schubert[1], S Abend[1], H Ahlers[1], W Ertmer[1], J Rudolph[2], J M Hogan[2], M A Kasevich[2], E M Rasel[1] and N Gaaloul[1]

[1] Institut für Quantenoptik and Centre for Quantum Engineering and Space-Time Research (QUEST), Leibniz Universität Hannover, Welfengarten 1, D-30167 Hannover, Germany
[2] Department of Physics, Stanford University, Stanford, CA 94305, United States of America

E-mail: gaaloul@iqo.uni-hannover.de

Keywords: atom interferometry, gravitational wave detection, inertial sensors, quantum gases, space physics, general relativity

Abstract

Recent proposals for space-borne gravitational wave detectors based on atom interferometry rely on extremely narrow single-photon transition lines as featured by alkaline-earth metals or atomic species with similar electronic configuration. Despite their similarity, these species differ in key parameters such as abundance of isotopes, atomic flux, density and temperature regimes, achievable expansion rates, density limitations set by interactions, as well as technological and operational requirements. In this study, we compare viable candidates for gravitational wave detection with atom interferometry, contrast the most promising atomic species, identify the relevant technological milestones and investigate potential source concepts towards a future gravitational wave detector in space.

1. Introduction

The first detection of gravitational waves [1], predicted by Einstein's theory of general relativity one hundred years ago, is without any doubt among the most exciting developments at the forefront of modern physics and holds the potential of routinely using gravitational wave antennas as an observational tool [2]. Beyond its significance as confirmation of general relativity predictions, the progress in establishing a network of gravitational wave observatories opens the path towards novel tools in astronomy. Indeed, it will enable the observation of previously undetectable phenomena [1], help gain insight into their event rates, correlate data analysis in multi-messenger astronomy campaigns [3], and allow for novel tests of the Einstein equivalence principle [4].

Ground-based laser interferometer detectors such as advanced VIRGO [5], advanced LIGO [6], GEO-600 [7], and others are designed to detect relatively weak, transient sources of gravitational waves such as coalescing black holes, supernovae, and pulsars in the frequency range of tens of Hz up to a few kHz. While significantly longer-lived and stronger sources such as galactic binaries, supermassive black hole binaries, and extreme mass ratio inspirals, emit gravitational waves at frequencies below 10Hz, these signals are masked on Earth by seismic and Newtonian noise when using state-of-the-art optical interferometers. Over the last decades, this has motivated the drive for space missions such as LISA pathfinder [8] and LISA [9] to perform millihertz-gravitational wave detection circumventing ground limits. Low-frequency gravitational waves below 10 Hz could be accessed in a terrestrial detector using freely falling atoms as test masses, that are decoupled from vibrational noise [10–14]. Gravity-gradient noise compensation concepts, using multiple atomic ensembles along a single baseline, can open up even lower frequency bands [15]. However, ground-based atom interferometers are also ultimately limited at frequencies approaching a fraction of a Hz and space-borne detectors are vital to probe the lowest frequencies [16].

In this article, we discuss methods for gravitational wave detection using matter-wave interferometry in space, assuming an experimental outline similar to the one recently reported in [17]. The scenario, which is based on the use of atom interferometry utilizing single-photon transitions [18–21], is assessed in view of available atomic species, demands on the atomic source, systematic effects, and the required environmental

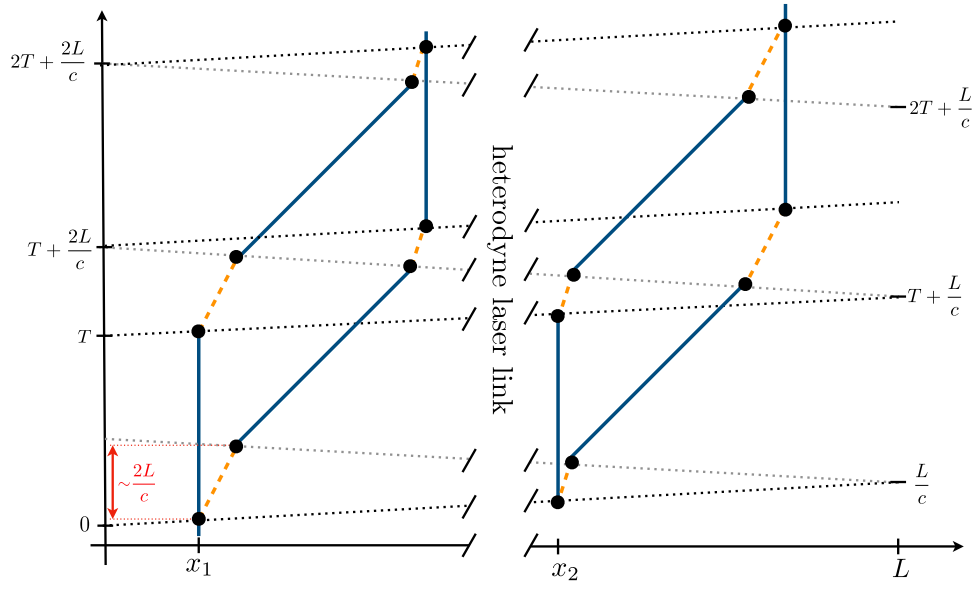

Figure 1. Interferometry scheme for a total momentum transfer $2\hbar k$ ($N = 1$) as described in [17, 19]. Atoms are prepared in the $^1S_0$ ground state (solid blue lines). Beam splitters and mirrors (dotted lines) using the $^1S_0 \rightarrow {}^3P_0$ clock transition are shared by two distant interferometers via coherent phase transfer and local repetition using a heterodyne laser link. During a single beam-splitter or mirror, the time spent in the excited state $^3P_0$ (dashed orange lines) $\sim 2L/c$ is dominated by photon travel time between the distant spacecraft.

control. A detailed trade-off study focusing on atomic source aspects as input for gravitational wave detectors has as of yet been missing.

2. Mission summary

The proposed sensor for low-frequency gravitational radiation exploits the differential phase shift of two inertially-sensitive atom interferometers on two spacecraft, separated by a baseline L. Such an atom interferometer scheme is proposed in [17, 19] and depicted in figure 1. The sequential absorption and stimulated emission of single photons on the $^1S_0 \rightarrow {}^3P_0$ clock transition (frequency ω_a) of a two-electron system allows the realization of effective $2\hbar k$ beam splitters. N sequentially applied beam splitters can address higher momentum states. The phase difference accumulated between the two interferometers under the influence of a passing gravitational wave with strain h, initial phase ϕ_0, and frequency ω reads

$$\Delta\phi = \frac{4N\omega_a}{c}\, h\, L \sin^2\left(\frac{\omega T}{2}\right)\sin(\phi_0 + \omega T), \tag{1}$$

growing linearly with increasing baseline as known from operation of gravity-gradiometers.

Laser phase noise requirements are mitigated in a differential measurement, since both gravimeters are operated with the same light, hence allowing for single baseline operation. In contrast to earlier proposals [19], a heterodyne laser link between the spacecraft allows to overcome previous limitations of the baseline L imposed by finite optical power and requirements on the link's collimation [17]. By locally repeating an incoming optical pulse and thus coherently transferring the interferometer phase over very large distances, baselines as suggested for LISA-like missions become accessible. The feasibility of the two scenarios proposed in [17] for different atomic sources is assessed in the following sections. The experimental arrangement consists in a baseline of $L = 2 \times 10^9$ m (6×10^8 m) with a maximum interrogation time $T = 160$ s (75 s) and beam splitting order $N = 1$ (6) yielding an expected maximum strain sensitivity of $< 10^{-19}$ $\mathrm{Hz}^{-1/2}$ ($< 10^{-20}$ $\mathrm{Hz}^{-1/2}$) around 10 mHz, meeting or even surpassing the expected LISA strain sensitivity.

3. Species assessment

3.1. Trade-off criteria

In this section we define and apply the criteria to identify an optimal species choice for the envisioned experiment. Desired properties can be summarized in the following three categories.

(i) *Electronic structure and narrow line transitions*—As the sensitivity of the proposed gravitational wave detector scales linearly with the effective wave number linked to the momentum ($\propto N\omega_a$) transferred onto the atomic wave packet, large transition frequencies are desired. Unlike the case of a small-scale experiment, the proposed single-photon beam splitting scheme studied here implies that the wave packets spend a non-negligible time, on the order of seconds, in the excited state (see figure 1). Consequently, this state has to have a lifetime significantly larger than $2L/c$ to overcome spontaneous emission, loss of coherence and deterioration of the output signal [22]. The obvious species considered here are typical optical clock atoms. Their two valence electrons can align parallel or anti-parallel, thus giving rise to a singlet and a triplet system. Naturally, dipole selection rules render electronic intercombination transitions forbidden and these transitions have narrow linewidths. In strontium e.g. this makes $^1S_0 \rightarrow {}^3P_1$ a favorable cooling transition due to the intimately related low Doppler cooling limit. The even further suppressed $^1S_0 \rightarrow {}^3P_0$ transition is consequently used in many optical atomic clocks, where spectroscopy on a mHz or narrower transition at a THz frequency is performed.

(ii) *Coherent excitation and ultra-low expansion rates*—Efficiently addressing an optical transition implies maintaining a good spatial mode overlap of the driving laser beam with the corresponding atomic ensemble. The Rabi frequency when driving a transition with linewidth Γ and saturation intensity $I_{\rm sat} = 2\pi^2\hbar c\Gamma/3\lambda^3$ reads

$$\Omega = \Gamma\sqrt{\frac{I}{2I_{\rm sat}}}. \tag{2}$$

Since the available laser intensity I is always finite, and especially limited on a spacecraft, small laser mode diameters and correspondingly even smaller atomic wave packet diameters are desired. The detector's frequency band of interest lies in the range of tens of millihertz, and hence the resulting evolution time T for maximum sensitivity is on the order of hundreds of seconds (equation (1)). During an interferometer time scale $2T$, the thermal expansion of an ensemble of strontium atoms at a temperature of 1 μK yields a cloud radius on the order of meters. As a direct consequence, cooling techniques to prepare atomic ensembles with the lowest possible expansion rates are required and heavier nuclei are in favor. Moreover, matter-wave collimation as realized in [23–25] is an indispensable tool to engineer the required weak expansion energies. Throughout the manuscript, we express this expansion energy in units of temperature and refer to it as the effective temperature $T_{\rm eff}$. For the purpose of this study, it lies typically in the picokelvin regime, which corresponds to few tens of μm s^{-1} of expansion velocity.

(iii) *Available technology and demonstration experiments*—Finally, any heritage from demonstration experiments is of importance when designing the sensor, especially in the scope of a space mission. Similarly, the availability of easy-to-handle reliable high-power laser sources with perspectives to develop space-proof systems are important criteria in the selection of an atomic species. As an example, laser wavelengths far-off the visible range should be avoided for the sake of simplicity, robustness, and mission lifetime.

In table 1, we provide an overview of available atomic species. While usually not occurring in atomic clocks, the proposed experimental arrangement requires the metastable state to be populated over time scales on the order of seconds or more. Within a single pair of sequential single-photon beam splitters, the time an atom spends in the excited state is $\sim 2L/c$ (dashed lines in figure 1), dominated by the light travel time between the two spacecraft. With an excited clock state decay rate Γ_0, a baseline L, and diffraction order N the remaining fraction of atoms in the interferometer reads

$$P_r = \exp\left[-\frac{4\,L\cdot N}{c}\cdot\Gamma_0\right]. \tag{3}$$

This loss of atoms by spontaneous emission[3] causes an increase in quantum projection noise by a factor of $1/\sqrt{P_r}$. In order to keep up the device's single-shot sensitivity, the atomic flux has to be increased accordingly or non-classical correlations have to be utilized to compensate for these losses. Similarly, when mitigating spontaneous losses via reduction of the instrument baseline or the beam splitting order, the linearly reduced sensitivity needs to be recovered with a quadratically larger atomic flux. As a result of their nuclear spins ($I \neq 0$), the electronic structure of fermionic species is subject to hyperfine interactions and has significantly larger clock linewidths than their bosonic counterparts [39]. Consequently, losses due to finite excited state lifetimes can significantly attenuate the signal for some species. Remaining atomic fractions after a full interferometer cycle for several fermionic isotopes are stated in table 2.

[3] Given the long pulse separation times on the order of hundreds of seconds, spontaneously decaying atoms will mostly drift away and not participate in the detection signal which can thus be expected to be near unity.

Table 1. Overview of possible two-electron systems featuring clock transitions. The isotopes treated in detail in this article are printed in boldface.

	Mass in u	$^1S_0 \rightarrow {}^3P_0$ linewidth $\Gamma_0/2\pi$ in Hz	Nat. abund.	$^1S_0 \rightarrow$ $^1P_1$ in nm	$^3P_1$ in nm	$^3P_0$ in nm	References
Fermions							
Mg	25	70×10^{-6}	10%	285	457	458	[26]
Ca	43	350×10^{-6}	0.1%	423	657	659	[26, 27]
Sr	**87**	1.5×10^{-3}	7%	461	689	698	[28]
Cd	111	5×10^{-3}[a]	13%	228	325	332	[29]
Yb	**171**	8×10^{-3}	14%	399	556	578	[30]
Hg	199	100×10^{-3}	17%	185	254	266	[31]
Bosons							
Mg	24	403×10^{-9}[b]	79%	285	458	457	[32]
Ca	40	355×10^{-9}[b]	97%	423	657	659	[33]
Sr	**84**	459×10^{-9}[b]	0.6%	461	689	698	[34]
Cd	114	[c]	29%	228	325	332	[35]
Yb	**174**	833×10^{-9}[b]	32%	399	556	578	[36]
Hg	202	[c]	30%	185	254	266	[37]

Notes.

[a] Linewidth estimation [29].

[b] Linewidth achievable with external magnetic field as described below; Calculated using equation (5) and [38] assuming $B = 100$ G, $P = 1$ W, laser waist $w = 4\sigma_r$, atomic ensemble radius $\sigma_r = 6$ mm and expansion rate $T_{\text{eff}} = 10$ pK.

[c] Necessary coefficients for the calculation unknown to the authors.

Table 2. Fraction of remaining atoms after an interferometric cycle for the different fermionic isotopes under consideration.

Baseline L	Diffraction order N	^{25}Mg	^{43}Ca	^{87}Sr	^{111}Cd	^{171}Yb	^{199}Hg
2×10^9 m	1	0.99	0.94	0.78	0.43	0.26	5×10^{-8}
6×10^8m	6	0.98	0.90	0.64	0.22	0.09	8×10^{-14}

3.2. Single-pulse excitation rates

Using bosonic isotopes with theoretical lifetimes of thousands of years in the metastable state $^3P_0$ circumvents the losses described above but requires different experimental efforts. Indeed, unlike fermionic candidates, single-photon clock transitions in bosonic species are not weakly allowed through spin-orbit-induced and hyperfine interaction mixing [39] and the excited state lifetime is limited by two-photon $E1M1$-decay processes, hence typically lying in the range of picohertz [34, 39].

Accordingly, efficient manipulation on the clock transition for beam splitting depends on induced state-mixing by magnetic-field induced spectroscopy [38]. For example, such a magnetic quench allows to weakly mix the triplet states $^3P_0$ and $^3P_1$and thus increases the clock transition probability. Using the formalism described in [38], which holds for linear polarizations, it is possible to infer Rabi frequencies

$$\Omega_0 = \alpha \cdot \sqrt{I} \cdot B, \tag{4}$$

and corresponding effective clock linewidths

$$\Gamma_{0,\text{eff}} = \gamma \frac{\Omega_L^2/4 + \Omega_B^2}{\Delta_{32}^2}, \tag{5}$$

under the assumption that the external magnetic field is colinear to the laser polarization[4]. Here, γ denotes the decay rate of $^3P_1$, Δ_{32} is the splitting between the triplet states and Ω_L and Ω_B are the coupling Rabi frequencies induced by the laser and the static magnetic field, respectively. Supporting the concept of concurrent operation of multiple interferometers [17], the external fields can be limited in terms of spatial extent to distinct interaction zones.

[4] This field configuration deviates from the case generally used in two-photon interferometers where the quantization axis is parallel to the beam splitting axis.

Table 3. Compared single-pulse excitation probability of fermionic and bosonic strontium for different sizes of the atomic ensemble, assuming an expansion energy of $T_{\rm eff} = 10$ pK, a clock laser power of $P = 1$ W with optimized beam waist, and an external magnetic field of $B = 100$ G in the bosonic case.

	^{84}Sr	^{87}Sr	^{84}Sr	^{87}Sr	^{84}Sr	^{87}Sr
Ensemble size (mm)	1		10		20	
Rabi frequency (2π Hz)	111.0	780.3	17.2	148.7	8.6	106.5
Excited fraction	0.79	0.99	0.19	0.87	0.1	0.73

In order to induce homogeneous Rabi frequencies over the spatial extent of the atomic ensemble, a reasonable spatial overlap between the exciting beam and the atomic cloud is required. Given the long drift times in the order of seconds, the clouds reach sizes in the order of millimeters, necessitating even larger beam waists. In view of limited laser power in a space mission, the resulting low intensities lead to Rabi frequencies in the few hundred Hz range for fermions. Assuming a magnetic field of 100 G, the corresponding Rabi frequencies are in the order of a few Hz for bosons. Table 3 illustrates the orders of magnitude for the two isotopes of strontium. Generally, smaller cloud sizes are advantageous, favoring the use of colder, i.e. slowly expanding sources.

The excitation probability is intimately connected to the phase space properties of the atomic cloud. An intensity profile of the exciting beam that varies over the spatial extent of the ensemble induces a space-dependent Rabi frequency except when the laser beam is shaped to be spatially uniform [40, 41]. One can overcome it by an increased beam waist leading to a homogeneous but smaller Rabi frequency. On the other hand, the effective Rabi frequency associated to a beam splitting light of wave number k being $\Omega_{\rm eff}(r,\, v) = \sqrt{\Omega_0^2(r) + (k \cdot v)^2}$, large waists (at limited power) would cause the Doppler detuning $(k \cdot v)^2$ to become the dominant term in $\Omega_{\rm eff}(r, v)$ thereby making the process very sensitive to the velocity distribution of the atomic ensemble. A trade-off to find the optimal waist maximizing the number of excited atoms throughout the full sequence is made in each scenario presented in this study. The respective excitation probability is calculated [42] as

$$P_{exc} = 2\pi \int\int r\, f(v) n(r,\, t) \left(\frac{\Omega_0(r)}{\Omega_{\rm eff}(r,\, v)}\right)^2 \sin^2\left(\frac{\Omega_{\rm eff}(r,\, v)}{2}\, t\right) {\rm d}r{\rm d}v, \tag{6}$$

where $f(v)$ is the longitudinal velocity distribution, $\Omega_0(r)$ is the spatially-dependent Rabi frequency and $n(r, t)$ is the transverse atomic density distribution. The resulting excited fraction for typical parameters of this study and for one pulse can be found in table 3.

3.3. Full interferometer excitation rates

In order to calculate the total fraction of atoms left at the detected state at the end of the interferometric sequence, one has to successively evaluate the integral (6) for each pulse. Indeed, the first light pulse selects a certain area in the ensemble's phase space distribution. The resulting longitudinal velocity distribution $f_{\rm new}(v)$ is computed and will constitute the input of the integral (6) relative to the next pulse. This treatment is iterated over the full pulses sequence of the considered scenarios. The long baseline scenario comprises $n_p = 7$ pulses while the short baseline scenario is realized by a sequence of $n_p = 47$ pulses. We illustrate, in figure 2, the short baseline case by showing, after each pulse, the new effective expansion temperature calculated after the new velocity width σ_{v_i}, the individual-pulse excitation rate $P_{{\rm exc},i}$ and the overall excitation probability at that point, given by the product of all previous pulses.

3.4. Residual detected atomic fraction

The total number of atoms detected at the interferometer ports is given, for each isotope, by evaluating the product of the excitation and the lifetime probabilities. In figure 3, we compile the outcome of these two studied aspects for the species considered in table 1. Assuming parameters that are well in line with state-of-the-art technology (filled symbols), i.e. an excitation field with $B = 100$ G, $P = 1$ W as well as an effective expansion temperature $T_{\rm eff} = 10$ pK and $\sigma_r = 6$ mm at the time of the matter wave lens, the plot suggests a preliminary trade-off. Although the bosons benefit from their small transition linewidths rendering them resilient to spontaneous decay, they all can only be weakly excited in the order of a few % or less (lower right corner of the figure). For clarity reasons, the isotopes that lie under an excitation probability of less than 0.5% are not represented. Heavier fermions, such as cadmium, mercury and ytterbium are subject to particularly large losses due to their broad linewidths (see table 2) in spite of very promising previous demonstration work in the case of ^{171}Yb [43]. It turns out that fermionic strontium and ytterbium are the most promising candidates, with a total fraction of around 12% of the atoms contributing to the interferometric signal in the long baseline scenario (circles), and around 10% in the case of strontium in the short baseline scenario (squares). Pushing the

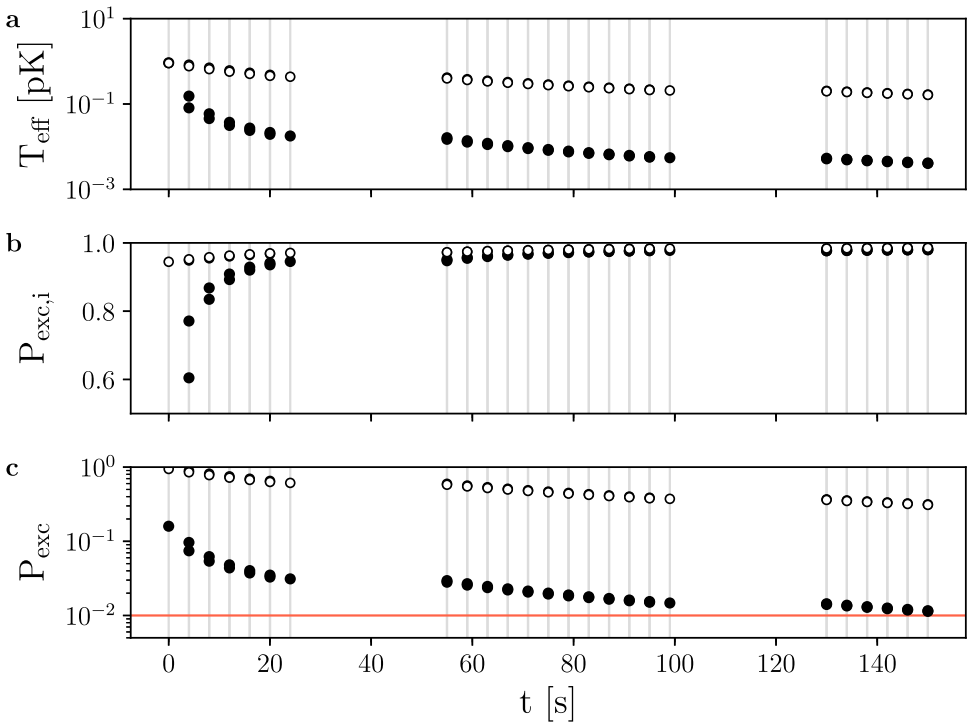

Figure 2. (a) Modified effective expansion temperature of an ensemble of ^{84}Sr after each pulse of the short-baseline scenario series of $n_p = 47$ pulses [17]. The filled (empty) circles refer to a quenching field of $B = 100$ G (500 G), a laser pulse power of $P = 1$ W (2 W) and a starting temperature $T_{\mathrm{eff},\,i} = 10$ pK (1 pK) for an ensemble with a width $\sigma_r = 6$ mm at the beginning of the interferometer. About half of the pulses are separated by $\Omega_{\mathrm{eff}}^{-1} < 1$ s which makes them indistinguishable at the scale of this plot. The faster expanding atoms (10 pK) experience a lower effective temperature after every pulse due to a smaller probability of excitation. (b) This excitation probability of every single pulse is plotted for values larger than 0.5. Due to the velocity selection, the ensemble is having a larger excitation rate with every pulse. (c) The probability product at each step stays above 1% (indicated by the red line) even for the less involving parameters choice (filled circles).

parameters to more ambitious values of $B = 500$ G, $P = 2$ W and $T_{\mathrm{eff}} = 1$ pK, improves the results significantly. In bosonic ytterbium and both isotopes of strontium, more than half of the atoms are left at the end of the pulse sequence of the long baseline scenario, and decent excitation rates are reached even in the short baseline configuration. Overall, ^{87}Sr turns out to be the most favorable isotope in this comparison.

3.5. Heritage

The worldwide efforts on demonstration experiments towards using the narrow clock transitions in Sr as a future frequency standard [28, 44] promises additional advantages of this choice through technological advances and research. In contrast, fermionic magnesium is difficult to address due to the ultraviolet singlet line, the weak cooling force of the $^1S_0 \rightarrow {}^3P_1$ transition [45] and quantum degeneracy not being demonstrated thus far. Likewise, trapping of fermionic calcium has only sparsely been demonstrated [27] and the intercombination cooling force is almost as weak as in the case of magnesium. Cooling techniques can be applied to all candidate bosons and finite clock transition linewidths can be achieved through magnetic field induced state mixing. A selection of a bosonic species would thus be motivated by previous demonstration experiments despite the weak excitation probability. In contrast, magnesium and calcium isotopes are missing simple paths to quantum degeneracy as a starting point for picokelvin kinetic energies. Although Bose–Einstein condensation has been shown for ^{40}Ca [33], the scheme is not particularly robust and the scattering length of 440 a_0 inhibits long-lived Bose–Einstein condensates (BEC). For cadmium, only magneto-optical trapping has been demonstrated [35]. Next to missing pathways to quantum degeneracy, its transition lines lie in the ultraviolet range. Mercury atoms can be ruled out for the same reason, although significant experience is available [37]. Additional candidates with convincing heritage are ^{174}Yb [46, 47] and ^{84}Sr, which has been brought to quantum degeneracy with large atom numbers in spite of its low abundance [48].

To conclude this section, we remark that the bosonic and fermionic isotopes of Yb and Sr are the most favorable when it comes to the number of atoms involved in the interferometric measurement. This holds for all scenarii considered: short and long baselines, modest and ambitious parameters and their combinations. We, therefore, pursue this trade-off focusing on these elements. We analyze their suitability for the use in the

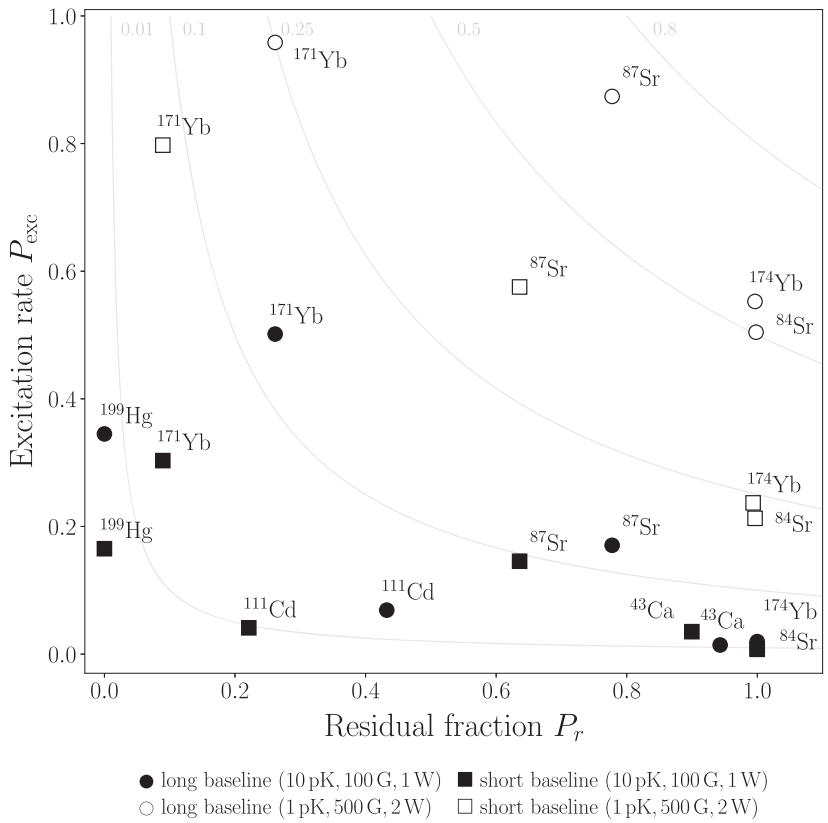

Figure 3. Residual atomic fraction, for the full sequence of pulses, in the long (circles) and short (squares) baseline scenarios for two different parameter sets: $T_{\text{eff}} = 10$ pK, $B = 100$ G and $P = 1$ W (filled symbols) and $T_{\text{eff}} = 1$ pK, $B = 500$ G and $P = 2$ W (empty symbols). The coordinates of each isotope reflect the residual fraction P_r of atoms left after accounting for spontaneous emission and the total excitation rate P_{exc} that can be achieved. Species with an excitation probability below the 0.5% rate (lower right corner), are not represented for clarity. Moreover, the most promising species, Yb and Sr, are computed with the more ambitious parameters set, which does not only shift the bosonic candidates into the feasible range but also yields promising results for the short baseline scenario.

proposed gravitational wave detector by considering the respective laser sources requirements and the necessary environmental control to constrain systematic effects.

4. Available laser sources

In this section, we discuss the technological feasibility to use the four most promising isotopes ^{84}Sr, ^{87}Sr, ^{171}Yb and ^{174}Yb in the proposed mission scheme. In terms of available laser technology, both elements are commonly used as sources in laboratory grade optical clocks, as well as considered to be interesting candidates for use in space missions with optical clocks [49]. Concerning the laser sources necessary to cool and manipulate both species, previous work has been performed for space qualification, mostly relying on diode laser systems [50]. Beyond the scope of this previous work, we want to discuss the possibilities for lattice-based atomic transport to isolate the preparation and detection zones from the interferometry region. The laser lines for the cooling transitions and their properties are listed in table 4.

In the laboratory environment, Zeeman slowers are routinely employed and a commercial compact source was recently presented for strontium [51], whose design can be adapted to ytterbium as well. For pre-cooling on the singlet transition at the UV wavelength 461 nm (399 nm) for Sr (Yb), fully free space coupled diode laser systems exist [49–51]. A possible alternative would be higher-harmonics generation of mid-IR fiber laser systems, which are robust and benefit from a large selection of commercially available sources.

To generate the 399 nm wavelength, a fiber laser for ytterbium would need two doubling stages starting from the infrared and thus requires high laser power in the IR. While the required fundamental wavelength for such a system is only slightly out of range of commercial fiber lasers, the strontium singlet line lies in an unsuitable range for second or even fourth harmonic generation with fiber lasers. As an alternative, tapered amplifiers are available at both fundamental frequencies to amplify the laser light.

The triplet transition for strontium at 689 nm can also be addressed by diode lasers [49]. While one does not require large power on this line due to its narrow linewidth in the kilohertz regime, the laser frequency needs to be stabilized using a stable optical cavity and a modulation scheme as well as a second 'stirring' laser are

Table 4. Laser lines and their properties for ^{84}Sr, ^{87}Sr, ^{171}Yb and ^{174}Yb as well as possible wavelengths for an optical dipole trap (ODT).

Laser line	^{84}Sr and ^{87}Sr			^{171}Yb and ^{174}Yb		
	λ	$\Gamma/2\pi$	I_{sat}	λ	$\Gamma/2\pi$	I_{sat}
Singlet	461 nm	30 MHz	10 mW cm^{-2}	399 nm	25 MHz	66 mW cm^{-2}
Triplet	689 nm	7.4 kHz	3 μW cm^{-2}	556 nm	182 kHz	0.14 mW cm^{-2}
Clock	698 nm	see section 3.1		578 nm	see section 3.1	
ODT	1 μm, 1.5 μm or 2 μm					

commonly used [52]. The required stability is relaxed for the triplet line for ytterbium lying at 556 nm due to the factor of 20 larger linewidth. It is accessible using frequency-doubled fiber laser systems, which have been developed for space applications [50, 53]. For trapping, evaporative cooling to quantum degeneracy, and matter wave lensing, fiber laser systems in the mid-IR, e.g. erbium-doped fiber lasers at 1 μm [54] or thulium-doped fiber lasers at 2 μm [55], can be employed.

More stringent requirements on the lasers are set by beam splitting on the clock transitions as discussed in the previous section. The same laser technology as for the triplet transitions is available for driving the clock transitions of both species at 698 nm and 578 nm, respectively, as their wavelengths only differ from the triplet transition by a few tens of nanometers. The suitable laser power on the order of 1 W is more demanding than for cooling applications, but feasible by either tapered amplifiers or frequency doubled fiber amplifiers. Larger laser powers can be reached by combining a high power fiber amplifier and a resonant doubling cavity, which might further increase the attainable Rabi frequencies. The necessary linewidth for single photon excitation scales with the effective Rabi frequency [19]. In our case, according to table 3 this requires Hz to sub-Hz linewidths, which is feasible for robust and transportable state-of-the-art cavities with already Hz linewidths [56, 57].

The transport of atoms from the preparation zone onto the interferometry axis and into the detection region will be realized via coherent momentum transfer using Bloch oscillations in an optical lattice [58, 59]. This technique is well established and enables the efficient transfer of a large number of photon momenta by two-photon scattering, employed for example in recoil measurements [60] or to realize fountain geometries on ground [61, 62]. Bloch oscillations can be driven by coupling to an arbitrary optical transition already discussed for cooling. Two main loss mechanisms have to be considered during the transport in an optical lattice, namely spontaneous emission and Landau–Zehner tunneling. To suppress spontaneous scattering, a laser detuning Δ with respect to the single-photon transition on the order of $10^4-10^5\,\Gamma$ is needed. The larger detuning Δ will lead to reduced transfer efficiencies unless the laser power is increased. This requires additional amplification stages, which due to their broad bandwidth might be shared with the cooling lasers. An optical lattice coupling to the narrower triplet line for ytterbium would yield a factor of three reduction in needed laser power at constant detuning Δ compared to the singlet transition. In contrast, the needed laser power to address both lines in strontium is rather similar and even 20% smaller for the singlet transition.

5. Error budget and source requirements

Source parameters such as the number of atoms and residual expansion do not only affect the shot noise as defined in section 3.1, but can also introduce an additional noise contribution which is not common to the interferometers on the two satellites. Consequently, additional requirements have to be derived to maintain the anticipated performance in a given environment and are consolidated in table 5. The discussion in this section is based on the following assumptions: The strain sensitivity shall be comparable to the LISA scenario with a free evolution time $2T = 320$ s and an effective wave vector corresponding to two photon recoil momenta [17, 19]. The two satellites are trailing behind earth and are nadir pointing with respect to the Sun which corresponds to a rotation rate of the satellites of 2×10^{-7}rad s^{-1}. This rotation rate implies a maximum allowed velocity fluctuation of the center of the cloud. In order to constrain residual rotation contributions below 1 mrad/Hz$^{1/2}$ for example, a maximum expansion rate of $T_{\mathrm{eff}} = 10$ pK is allowed in the case of 4×10^7 atoms s^{-1}, when shot-noise-limited fluctuations are assumed. Spatial and velocity distributions are assumed to be isotropic and gaussian. The requirement on the initial rms-width of $\sigma_r = 6$ mm of the wave packet is defined by the necessity for a low density to suppress collisional shifts given an uncertainty of the first beam splitter of 0.1% [63]. Subsequently, the maximum gravity gradient is derived. The atom interferometer operates in the point source limit [61, 64] enabling the read-out of fringe patterns in the interferometer output ports due to gravity gradients. We approximate the interferometer geometry for short pulses when calculating the phase shifts [65, 66]. This does not strictly hold for the given scenario but gives the correct order of magnitude nonetheless.

Table 5. Requirements to reach phase noise contributions of 1 mrad/Hz$^{1/2}$ individually. Motion and position noise, $\sigma_v/\sqrt{N_a}$ and $\sigma_r/\sqrt{N_a}$, respectively, are considered to be shot-noise-limited.

	^{84}Sr	^{174}Yb
Initial radius σ_r	<6 mm	<6 mm
Temperature equivalent $T_{\rm eff}$	<10 pK	<10 pK
Final radius	<16 mm	<13 mm
Residual rotations Ω	$<2.2\times10^{-7}$ rad s^{-1}	$<2.6\times10^{-7}$ rad s^{-1}
Gravity gradients $\gamma_\parallel$ + velocity	$<2.7\times10^{-9}$ 1/s^2	$<3.3\times10^{-9}$ 1/s^2
Gravity gradients $\gamma_\parallel$ + position	$<2.3\times10^{-9}$ 1/s^2	$<1.9\times10^{-9}$ 1/s^2
Gravity gradients $\gamma_\perp$ + velocity	$<1.6\times10^{-5}$ 1/s^2	$<1.7\times10^{-5}$ 1/s^2
Gravity gradients $\gamma_\perp$ + position	$<7.8\times10^{-6}$ 1/s^2	$<5.7\times10^{-6}$ 1/s^2
Maximum wave front fluctuation σ_R	$<20\%\cdot 54$ km	$<12\%\cdot 54$ km

Residual rotations Ω coupled to a velocity uncertainty of the cloud $\sigma_v/\sqrt{N_a} = \sqrt{k_{\rm B}T_{\rm eff}/m}/\sqrt{N_a}$ with Boltzmann's constant $k_{\rm B}$, atomic mass m, and number N_a induce a phase fluctuation $\sigma_{\phi_{\rm rot}} = 2\,k\,\sigma_v\,\Omega\,T^2/\sqrt{N_a}$. A temperature equivalent of 10 pK leads to a shot noise limited cloud velocity uncertainty below 5 nm s^{-1} which is compatible with the anticipated noise limit.

The atoms mostly reside in the ground state (see figure 1), allowing for a straightforward estimation of the phase noise contribution due to collisions. The scattering length of the ground state of ^{174}Yb (^{84}Sr) is 105 a_0 (123 a_0) where a_0 is the Bohr radius [47, 48]. Any imperfection of the initial beam splitter induces a differential density between the two interferometer arms and consequently induces a noise contribution if fluctuating [63]. With an isotropic rms-width of 6mm at the time of the first beam splitter, an uncertainty in the beam splitting ratio of 0.1%, and an isotropic expansion corresponding to 10 pK, the phase uncertainty stays within a few 0.1 mrad.

Gravity gradients parallel to the sensitive axis $\gamma_\parallel$ and a center of mass velocity jitter induce a phase noise according to the formula $\sigma_{\phi_{v,\gamma,\parallel}} = k\,\gamma_\parallel\,\sigma_v\,T^3/\sqrt{N_a}$. Thus, the gravity gradient has to fulfill the condition $\gamma_\parallel < 2\times10^{-9}$ s^{-2}. A similar requirement is derived, when considering the cloud's shot noise limited position uncertainty $\sigma_r/\sqrt{N_a}$ using $\sigma_{\phi_{r,\gamma,\parallel}} = k\,\gamma_\parallel\,\sigma_r\,T^2/\sqrt{N_a}$.

Gravity gradients $\gamma_\perp$ perpendicular to the sensitive axis couple to the center of wave packet motion as well if a rotation is present. With the orbital frequency and the stated uncertainties in position and velocity, the maximum compatible gradient of $\sim6\times10^{-6}$ s^{-2} is deduced from $\sigma_{\phi_{v,\gamma,\perp}} = 14/3\,k\,\sigma_v\,\gamma_\perp\,\Omega\,T^4/\sqrt{N_a}$ and $\sigma_{\phi_{r,\gamma,\perp}} = 8\,k\,\sigma_r\,\gamma_\perp\,\Omega\,T^3/\sqrt{N_a}$.

A properly designed mass distribution will be necessary to reach this target and a distance to Earth of at least 7×10^7 m is required to keep Earth's gravity gradient below the threshold of $\sim2\times10^{-9}$ s^{-2} [17].

Finally, the finite expansion rate σ_v couples to the effective wave front curvature radius which induces the phase shift $\phi_{wf} = k\,T^2\,\sigma_v^2/R$ [67, 68]. Consequently, instabilities in the effective temperature $\sigma_{T_{\rm eff}}$ and effective wave front curvature radius σ_R lead to a phase noise of $\sigma_{\phi_{wf},T} = kT^2\,k_{\rm B}/(m\,R)\cdot\sigma_{T_{\rm eff}}$ and $\sigma_{\phi_{wf},R} = k\,T^2\,k_{\rm B}\,T_{\rm eff}/(m\,R^2)\cdot\sigma_R$, respectively[5]. Assuming an effective wavefront curvature radius $R = 54$ km corresponding to a peak-to-valley of $\lambda/30$ across a beam with a diameter of 10 cm, the fluctuations for ytterbium (strontium) have to be limited to $\sigma_{T_{\rm eff}} < T_{\rm eff}\cdot 20\%$ ($\sigma_{T_{\rm eff}} < T_{\rm eff}\cdot 10\%$) and $\sigma_R < R\cdot 20\%$ ($\sigma_R < R\cdot 12\%$).

6. Regimes of temperature and density

6.1. Expansion dynamics

The error model devised in the previous section assumes a different size of the atomic cloud at different steps of the experimental sequence. The expansion dynamics relies decisively on the temperature and densities considered. Depending on these parameters, bosonic gases, assumed to be confined in harmonic trapping potentials, are found in different possible regimes. Here, we treat Bose–Einstein condensed gases as well as non-degenerate ensembles in all collisional regimes ranging from the collisionless (thermal) to the hydrodynamic limit. We comment on the analogy with fermions later in this section.

The phase-space behavior of ensembles above the critical temperature of condensation is well described by the Boltzmann–Vlasov equation in the collisionless and hydrodynamic regimes [69, 70], whereas the mean-field dynamics of a degenerate gas are captured by the time-dependent Gross–Pitaevskii equation [71]. However, gases released from a harmonic confinement, experience a free expansion that can conveniently be rendered by

[5] $\sigma_{T_{\rm eff}}$ effectively denotes the instability in the expansion rate σ_v.

simple scaling theories. In this approach, the gas is assumed to merely experience a dilation after release with an unchanged shape but a size $L_i(t)$ evolving according to

$$L_i(t) = b_i(t) L_i(0), \tag{7}$$

with $L_i(0)$ being the initial (in-trap) size and i denoting the spatial coordinate x, y or z. The dynamics in time are accounted for by the scaling parameters $b_i(t)$, which interpolate between all collisional regimes of non-degenerate (bosonic[6]) gases in reference [70] and for degenerate gases of bosons in [72, 73]. The initial size $L_i(0)$ depends on the interaction and temperature regime of the gas.

In the thermal non-interacting case, the initial size corresponds to the rms-width $\sigma_i^{\mathrm{th}}(0) = \sqrt{k_{\mathrm{B}} T_a / m\omega_i^2}$ of the Gaussian density distribution trapped with the angular frequency ω_i in the direction i at a temperature T_a [74], the atomic mass m and the Boltzmann constant k_{B}. Considering elastic interactions, the initial size is a correction of the collisionless rms-width with a modified trapping frequency $\tilde{\omega}_i^2 = \omega_i^2(1 - \xi)$ accounting for the mean-field E_{mf} via the parameter $\xi = E_{\mathrm{mf}}/(E_{\mathrm{mf}} + k_{\mathrm{B}} T_a)$ [75]. In the bosonic case, E_{mf} equals $2gn$, with the density of the cloud n and the interaction strength $g = 4\pi\hbar^2 a_s/m$ for an s-wave scattering length a_s and the the modified Planck constant $\hbar$. BECs are, on the other hand, well represented with a parabolic shape in the Thomas–Fermi regime for a large number of particles (the study case here). Their size is hence parametrized with the Thomas–Fermi-radius $R_i(0) = \sqrt{2\mu/m\omega_i^2}$, where μ is the chemical potential of the degenerate gas [71]. Although the physical origin is different, trapped Fermions display a similar density distribution as the interacting bosons. The Thomas–Fermi radii $R_i(0) = \sqrt{2E_{\mathrm{F}}/m\omega_i^2}$ are determined by the Fermi-energy E_{F} [76].

6.2. Delta-kick collimation

Having defined the initial sizes for the different regimes of interest, we obtain the size at time t by solving the differential equations for the scaling parameters $b_i(t)$ following the treatment in [72, 73] for condensed and in [70] for non-degenerate gases in all collisional regimes. The result is illustrated in figures 4(a) and (c) in the case of ^{84}Sr and ^{87}Sr. The free expansion of the cloud in the different regimes is in each case plotted for times smaller than t_{DKC} denoting the application time of a delta-kick collimation (DKC) pulse. This pulse consists in re-flashing the initial trap causing a collimation of the atomic cloud [23, 24]. In the case of fermionic atoms populating a single-spin state, the cloud's expansion behavior is similar to that of a non-interacting (thermal) bosonic ensemble [76]. However, for a superposition of hyperfine states, s-wave scattering interactions are possible and the phase diagram of such gases is very rich leading to different expansion laws ranging from collisionless to hydrodynamic, BCS or unitary behavior [77]. DKC of molecular BECs [78] would give results similar to the atomic BEC case. For simplicity, we restrict the dynamics study (expansion and DKC) to the bosonic and single-spin-component fermionic cases keeping in mind that similar results can be retrieved for a superposition of hyperfine states in a fermionic ensemble. Different considerations in this study would therefore be more decisive for the bosons/fermions trade-off.

In the absence of interactions, the physics of an expanding cloud is captured by the Liouville's theorem (phase-space density conservation) and reads

$$\sigma_{v_{f,i}} \sigma_{f,i} = \sigma_{v_{0,i}} \sigma_{0,i}, \tag{8}$$

$\sigma_{0,i} = \sigma_i^{\mathrm{th}}{}_i(0)$ and $\sigma_{v_{0,i}} = \sqrt{k_{\mathrm{B}} T_a/m}$ being the initial size and velocity widths of a thermal cloud, respectively, and $\sigma_{f,i} = \sigma_i^{\mathrm{th}}{}_i(t_{\mathrm{DKC}})$ is the size when the lens is applied. Evaluating this expression thus yields the minimum cloud size required at the delta-kick to achieve a certain target temperature performance T_{eff}. However, interactions affect the free expansion of the cloud (hence the time of free expansion needed to reach the required size at the kick) and the residual velocity width after application of the lens. For non-degenerate gases we account for this by choosing the following ansatz for the phase-space distribution f of the ensemble:

$$f(t_{\mathrm{DKC}} + \tau, x_i, v_i) = f(t_{\mathrm{DKC}}, x_i, v_i - \omega_i^2 \tau x_i). \tag{9}$$

This approach, which is inspired by the treatment in [79], assumes that the duration τ of the lens is very small compared to the time of free expansion, such that the spatial distribution is left unchanged while the momentum is changed instantaneously by $\delta p_i = -m\omega_i^2 \tau x_i$ when the harmonic lens potential is applied. This, combined with the free expansion of interacting, non-degenerate gases [70], gives rise to the momentum width

$$\sigma_{v_{f,i}} = \sigma_{v_{0,i}} \theta_i^{1/2}(t_{\mathrm{DKC}}) \tag{10}$$

after a lens which satisfies the condition $\dot{b}_i(t_{\mathrm{DKC}}) = \tau\omega_i^2 b_i(t_{\mathrm{DKC}})$. The scaling parameters θ_i are the time-evolved effective temperatures in each direction and are determined, similarly to the spatial scaling parameters b_i, by solving the differential equations in [70]. It is worth noticing that this general treatment leads to equation (8) in the non-interacting case, which we also use to assess the delta-kick performance of a degenerate Fermi gas in one spin state (where interactions are absent [76]).

[6] In fact, they are also valid for a Fermi gas in its normal phase.

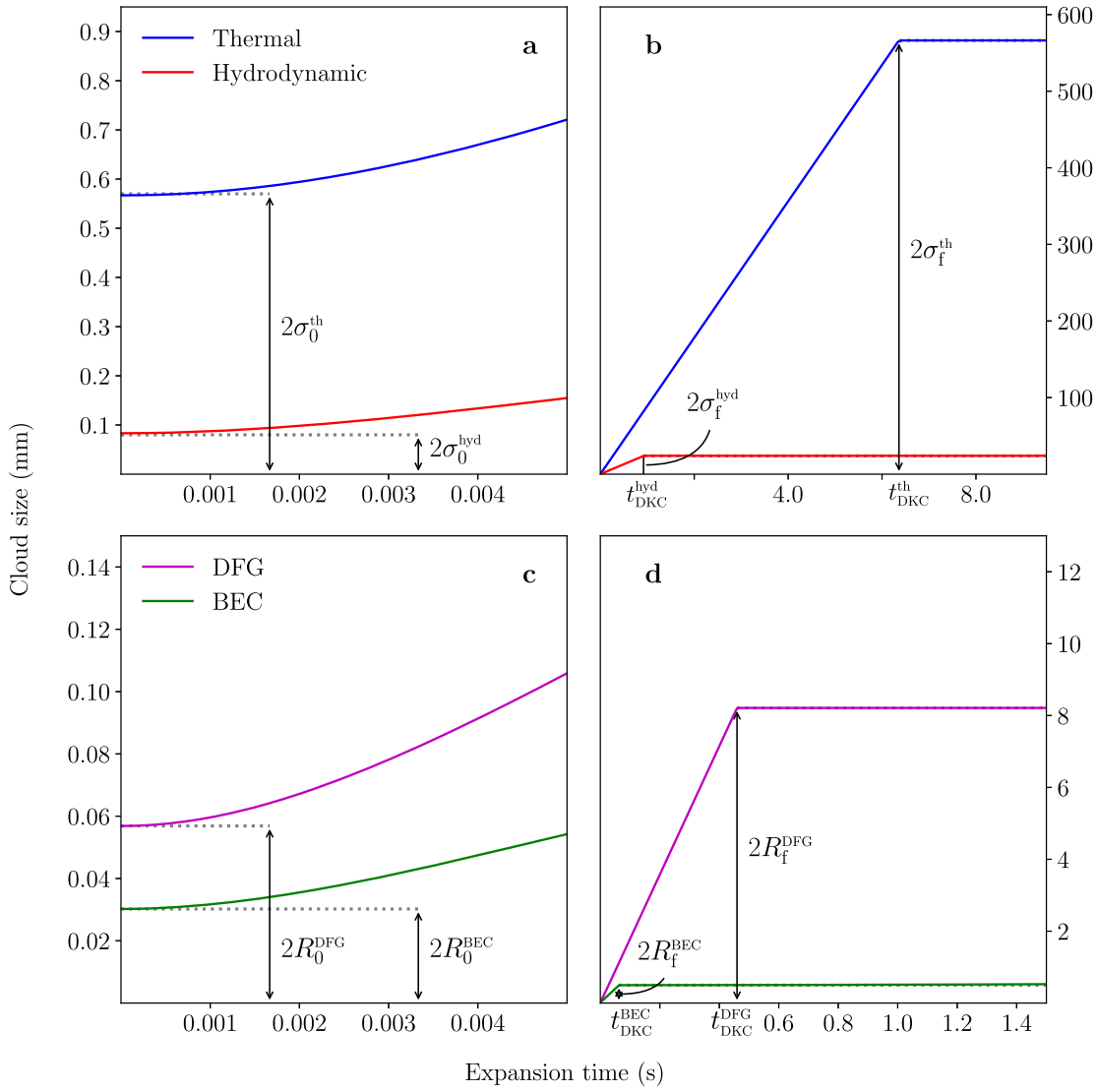

Figure 4. Full size of the ensembles in different regimes for the parameters specified in tables 6 and 7 before and after the delta-kick collimation pulses. (a) Sizes of the bosonic ^{84}Sr cloud at the beginning of the free expansion (up to 5 ms) for the thermal (blue) and hydrodynamic (red) regimes. The full sizes at the release are indicated for both. (b) Sizes of the bosonic ^{84}Sr cloud for the total duration of the free expansion (up to 10 s) for the thermal (blue) and hydrodynamic (red) regimes. The full sizes at the DKC pulse are indicated for both. (c) Sizes of the ^{84}Sr BEC (green) and the fermionic degenerate gas of ^{87}Sr (purple) at the beginning of the free expansion (up to 5 ms). The full sizes at the release are indicated for both. (d) Sizes of the ^{84}Sr BEC (green) and the fermionic degenerate gas of ^{87}Sr (purple) for the total duration of the free expansion (up to 10 s). The full sizes at the DKC pulse are indicated for both. The size is defined as the Gaussian rms-width in the case of the thermal and hydrodynamic regimes and as the Thomas–Fermi radius in the degenerate cases. The full size is in both cases a simple multiplication by a factor 2.

For BECs at zero temperature, the previous models can not be applied anymore. We employ, instead, an energy conservation model which assumes that the energy due to repulsive atomic interactions converts into kinetic energy during free expansion at a first stage. The asymptotic three-dimensional expansion rate Δv_f after the delta-kick, in this model, stems from the residual mean-field energy and a Heisenberg term $\propto \hbar^2/mR_f^2$, which dominates for larger time of flights when the mean-field energy has dissipated. It reads

$$\Delta v_f = \left(\frac{5N_a g}{2m\pi R_f^3} + \frac{14\hbar^2}{3mR_f^2} \right)^{1/2}, \tag{11}$$

with N_a being the number of atoms and $R_f = R(t_{\rm DKC})$ being the size at lens [71]. We relate this expansion rate to an effective temperature via $\frac{3}{2}k_{\rm B}T_{\rm eff} = \frac{m}{2}(\Delta v_f/\sqrt{7})^2$ [25, 80] and restrict ourselves to the isotropic case for simplicity.

After the application of the delta-kick pulse, we assume a linear expansion during the interferometry sequence lasting $2T$. The full size $L(2T)$ of the cloud at the end of the sequence is then given in all regimes by

Table 6. Ensembles sizes compatible with the 10 pK expansion rate requirement for classical gases in the collisionless and hydrodynamic regimes. The characteristics of the considered experimental arrangement are stated in the six first rows of the table. The computed resulting sizes are given, after the treatment of section 6.2, in the next rows. Of particular importance for the trade-off performed in this paper, are the sizes at lens (bold) and the final detected sizes for several interferometry times $2T$. The larger these sizes, the harsher the requirements are on the DKC and interferometry pulses.

3D expansion rate $T_{\rm eff} = 10$ pK	Collisionless		Hydrodynamic	
	^{174}Yb	^{84}Sr	^{174}Yb	^{84}Sr
Number of atoms	5×10^8		5×10^7	
Trapping frequency (2π Hz)	25		50	
Initial temperature (μK)	10		0.83	
Initial size $2\sigma_0$ (μm)	393.77	566.91	58.03	83.22
Knudsen number [75]	0.28	0.42	0.06	0.09
Phase space density	$<10^{-3}$		0.6	
Pre-DKC expansion time ($t_{\rm DKC}$) (ms)	6359		924	
Size at lens $2\sigma(t_{\rm DKC})$ (mm)	**393.32**	**566.27**	**16.73**	**23.99**
Final size $2\sigma\,(t_{\rm DKC} + 2T)$ (mm)				
$T = 40$ s	393.34	566.29	17.09	24.51
$T = 100$ s	393.42	566.41	18.88	27.09
$T = 160$ s	393.57	566.63	21.81	31.33

Table 7. Ensembles sizes compatible with the 10 pK expansion rate requirement for quantum degenerate regimes. The entries of the table are the same than 6. For BECs and DFGs the computed sizes are dramatically smaller than the thermal counterparts.

3D expansion rate $T_{\rm eff} = 10$ pK	BEC		DFG	
	^{174}Yb	^{84}Sr	^{171}Yb	^{87}Sr
Number of atoms	7×10^6		7×10^6	
Trapping frequency (2π Hz)	50		50	
Critical temperature (μK)	0.431		0.834	
Initial size $2R_0$ (μm)	30.2	41.8	56.86	81.86
Pre-DKC expansion time ($t_{\rm DKC}$) (ms)	63	61	460	460
Size at lens $2R(t_{\rm DKC})$ (mm)	**0.50**	**0.67**	**8.21**	**11.82**
Final size $2R\,(t_{\rm DKC} + 2T)$ (mm)				
$T = 40$ s	9.27	13.34	12.86	18.51
$T = 100$ s	23.15	33.32	26.07	37.53
$T = 160$ s	37.03	53.31	40.43	58.20

$$L(2T) = 2\sqrt{L_f^2 + (2T\Delta v)^2}\,, \tag{12}$$

with $L_f = \sigma_f$, $\Delta v = \sigma_{v_f}$ in the non-degenerate regimes and $L_f = R_f$, $\Delta v = \Delta v_f$ for condensed ensembles. In what follows, indices relative to spatial directions are left since we, for simplicity, chose to treat isotropic cases. With the models adopted above, we show in the tables 6 (non-degenerate gases) and 7 (quantum degenerate ensembles) the characteristic figures for the various regimes for a given asymptotic target expansion temperature of 10 pK. The minimum required cloud sizes are printed in bold and are depicted in figures 4(b) and (d), along with the size at the end of the interferometric sequence. The extent over which state-of-the art magnetic and optical potentials can be considered harmonic is typically limited to a few mm in the best case. This operating range is a decisive criterion for the choice of the initial cloud temperature and density configuration.

As a conclusion to this section with respect to the required size at lens, we find out that degenerate ensembles thanks to their point-like initial extension are largely favored. The availability of traps with significantly larger harmonic extent could eventually make the use of a non-degenerate gas in the hydrodynamic regime feasible in the future. Another possibility in to use classical gases through a velocity selection stage, which, however, is always accompanied by a substantial loss of atoms and typically reduces the velocity spread in one dimension only.

7. Conclusion

In this paper, we have exposed the necessary criteria for choosing the atomic source of a space-borne gravitational wave observatory mission scenario [17]. In that scenario, featuring a baseline $L = 2 \times 10^9$ m (6×10^8 m) and a maximum interrogation time $T = 160$ s (75 s), the use of beam splitting order $N = 1$ (6) yields a maximum strain sensitivity of $< 10^{-19}$ Hz$^{-1/2}$ ($< 10^{-20}$ Hz$^{-1/2}$) around 10 mHz, comparable to the expected LISA strain sensitivity. ^{87}Sr, ^{84}Sr, ^{174}Yb and ^{171}Yb seem to be the most promising candidates in light of their fundamental properties, technical feasibility, and availability of laser sources. Further atomic losses due to the finite excitation rates will have to be mitigated by either enhancing the field parameters through increased laser power and/or stronger static magnetic fields in the case of the bosons or by optimizing the source by achieving even lower expansion rates with longer free expansion time prior to the atomic lens. We constrained the implementation parameters by an error model incorporating source expansion dynamics and interferometric phase shifts. Looking closer at the atomic source properties, it is shown that by the appropriate choice of a quantum-degenerate expansion regime, the assumed expansion performance of 10 pK can be met after a DKC treatment. While further experimental development is necessary to meet the atomic flux requirements of 4×10^7 atoms s^{-1}, recent robust BEC production in microgravity [81] and space [82] demonstrate important steps towards meeting this goal. In general, the exploration of cold atom technologies in microgravity [23, 83, 84] and in space [85, 86] is a promising and rapidly progressing field of research.

Acknowledgments

The authors acknowledge financial support from DFG through CRC 1227 (DQ-mat), project B07. The presented work is furthermore supported by CRC 1128 (geo-Q), the German Space Agency (DLR) with funds provided by the Federal Ministry of Economic Affairs and Energy (BMWi) due to an enactment of the German Bundestag under Grants No. 50WM1641, 50WM1952, 50WP1700 and 50WM1435. Furthermore, support of the 'Niedersächsisches Vorab' through the 'Quantum- and Nano-Metrology' (QUANOMET) initiative within the project QT3 is acknowledged as well as through 'Förderung von Wisenschaft und Technik in Forschung und Lehre' for the initial funding of research in the new DLR institute. Moreover, networking support by the COST action CA16221 'Atom Quantum Technologies' and the Q-SENSE project funded by the European Union's Horizon 2020 Research and Innovation Staff Exchange (RISE) under Grant Agreement Number 691156 is acknowledged. SL acknowledges mobility support provided by the IP@Leibniz program of the LU Hanover. DS gratefully acknowledges funding by the Federal Ministry of Education and Research (BMBF) through the funding program Photonics Research Germany under contract number 13N14875. Robin Corgier, David Guéry-Odelin, Nandan Jha, Jan-Niclas Siemß and Klaus Zipfel are gratefully acknowledged for their valuable discussions and comments. The publication of this article was funded by the Open Access Fund of the Leibniz Universität Hannover.

ORCID iDs

S Loriani https://orcid.org/0000-0001-6660-960X
J M Hogan https://orcid.org/0000-0003-1218-2692
N Gaaloul https://orcid.org/0000-0001-8233-5848

References

[1] Abbott B P *et al* 2016 *Phys. Rev. Lett.* **116** 061102
[2] Abbott B P *et al* 2016 *Phys. Rev. Lett.* **116** 241103
[3] Nissanke S, Kasliwal M and Georgieva A 2013 *Astrophys. J.* **767** 124
[4] Wu X F, Gao H, Wei J J, Mészáros P, Zhang B, Dai Z G, Zhang S N and Zhu Z H 2016 *Phys. Rev.* D **94** 024061
[5] Acernese F *et al* 2015 *Class. Quantum Grav.* **32** 024001
[6] Aasi J *et al* 2015 *Class. Quantum Grav.* **32** 074001
[7] Affeldt C *et al* 2014 *Class. Quantum Grav.* **31** 224002
[8] Armano M *et al* 2016 *Phys. Rev. Lett.* **116** 231101
[9] Danzmann K *et al* 2011 *ESA Report No. ESA/SRE(2011)3*
[10] Dimopoulos S, Graham P W, Hogan J M, Kasevich M A and Rajendran S 2008 *Phys. Rev.* D **78** 122002
[11] Delva P and Rasel E M 2009 *J. Mod. Opt.* **56** 1999
[12] Hohensee M, Lan S Y, Houtz R, Chan C, Estey B, Kim G, Kuan P C and Müller H 2010 *Gen. Relativ. Gravit.* **43** 1905
[13] Hogan J M *et al* 2011 *Gen. Relativ. Gravit.* **43** 1953
[14] Chiow S W, Williams J and Yu N 2015 *Phys. Rev.* A **92** 063613
[15] Chaibi W, Geiger R, Canuel B, Bertoldi A, Landragin A and Bouyer P 2016 *Phys. Rev.* D **93** 021101
[16] Graham P W, Hogan J M, Kasevich M A, Rajendran S and Romani R W 2017 arXiv:1711.02225

[17] Hogan J M and Kasevich M A 2016 *Phys. Rev.* A **94** 033632
[18] Yu N and Tinto M 2010 *Gen. Relativ. Gravit.* **43** 1943
[19] Graham P W, Hogan J M, Kasevich M A and Rajendran S 2013 *Phys. Rev. Lett.* **110** 171102
[20] Hu L, Poli N, Salvi L and Tino G M 2017 *Phys. Rev. Lett.* **119** 263601
[21] Norcia M A, Cline J R K and Thompson J K 2017 *Phys. Rev.* A **96** 042118
[22] Bender P L 2014 *Phys. Rev.* D **89** 062004
[23] Müntinga H *et al* 2013 *Phys. Rev. Lett.* **110** 093602
[24] Kovachy T, Hogan J M, Sugarbaker A, Dickerson S M, Donnelly C A, Overstreet C and Kasevich M A 2015 *Phys. Rev. Lett.* **114** 143004
[25] Rudolph J 2016 Matter-wave optics with Bose–Einstein condensates in microgravity *PhD Thesis* Leibniz Universität Hannover
[26] Porsev S G and Derevianko A 2004 *Phys. Rev.* A **69** 042506
[27] Moore I D, Bailey K, Greene J, Lu Z T, Müller P, O'Connor T P, Geppert C, Wendt K D A and Young L 2004 *Phys. Rev. Lett.* **92** 153002
[28] Falke S *et al* 2014 *New J. Phys.* **16** 073023
[29] Gibble K 2015 private communication
[30] Sherman J A, Lemke N D, Hinkley N, Pizzocaro M, Fox R W, Ludlow A D and Oates C W 2012 *Phys. Rev. Lett.* **108** 153002
[31] Yi L, Mejri S, McFerran J J, Le Coq Y and Bize S 2011 *Phys. Rev. Lett.* **106** 073005
[32] Kulosa A P *et al* 2015 *Phys. Rev. Lett.* **115** 240801
[33] Kraft S, Vogt F, Appel O, Riehle F and Sterr U 2009 *Phys. Rev. Lett.* **103** 130401
[34] Santra R, Christ K V and Greene C H 2004 *Phys. Rev.* A **69** 042510
[35] Brickman K A, Chang M S, Acton M, Chew A, Matsukevich D, Haljan P C, Bagnato V S and Monroe C 2007 *Phys. Rev.* A **76** 043411
[36] Barber Z W, Hoyt C W, Oates C W, Hollberg L, Taichenachev A V and Yudin V I 2006 *Phys. Rev. Lett.* **96** 083002
[37] Petersen M, Chicireanu R, Dawkins S T, Magalhães D V, Mandache C, Le Coq Y, Clairon A and Bize S 2008 *Phys. Rev. Lett.* **101** 183004
[38] Taichenachev A V, Yudin V I, Oates C W, Hoyt C W, Barber Z W and Hollberg L 2006 *Phys. Rev. Lett.* **96** 083001
[39] Boyd M M, Zelevinsky T, Ludlow A D, Blatt S, Zanon-Willette T, Foreman S M and Ye J 2007 *Phys. Rev.* A **76** 022510
[40] Gaunt A L, Schmidutz T F, Gotlibovych I, Smith R P and Hadzibabic Z 2013 *Phys. Rev. Lett.* **110** 200406
[41] Mielec N, Altorio M, Sapam R, Horville D, Holleville D, Sidorenkov L A, Landragin A and Geiger R 2018 *Appl. Phys. Lett.* **113** 161108
[42] Cheinet P 2006 Conception et réalisation d'un gravimètre atomes froids *PhD Thesis* SYRTE
[43] Taie S, Takasu Y, Sugawa S, Yamazaki R, Tsujimoto T, Murakami R and Takahashi Y 2010 *Phys. Rev. Lett.* **105** 190401
[44] Nicholson T *et al* 2015 *Nat. Commun.* **6** 6896
[45] Mehlstäubler T 2005 Neuartige Kühlmethoden für einen optischen Magnesium Frequenzstandard *PhD Thesis* Leibniz Universität Hannover
[46] Takasu Y, Honda K, Komori K, Kuwamoto T, Kumakura M, Takahashi Y and Yabuzaki T 2003 *Phys. Rev. Lett.* **90** 023003
[47] Roy R, Green A, Bowler R and Gupta S 2016 *Phys. Rev.* A **93** 043403
[48] Stellmer S, Grimm R and Schreck F 2013 *Phys. Rev.* A **87** 013611
[49] Bongs K *et al* 2015 *C.R. Phys.* **16** 553
[50] Schiller S *et al* 2012 *European Frequency and Time Forum (EFTF), 2012* (Piscataway, NJ: IEEE) pp 412–8
[51] AOSense. web http:/aosense.com/
[52] Mukaiyama T, Katori H, Ido T, Li Y and Kuwata-Gonokami M 2003 *Phys. Rev. Lett.* **90** 113002
[53] MenloSystems. web http://menlosystems.com/
[54] Adams C S, Lee H J, Davidson N, Kasevich M and Chu S 1995 *Phys. Rev. Lett.* **74** 3577
[55] Hartwig J, Abend S, Schubert C, Schlippert D, Ahlers H, Posso-Trujillo K, Gaaloul N, Ertmer W and Rasel E M 2015 *New J. Phys.* **17** 035011
[56] Leibrandt D R, Thorpe M J, Bergquist J C and Rosenband T 2011 *Opt. Express* **19** 10278
[57] Parker B, Marra G, Johnson L A M, Margolis H S, Webster S A, Wright L, Lea S N, Gill P and Bayvel P 2014 *Appl. Opt.* **53** 8157
[58] Ben Dahan M, Peik E, Reichel J, Castin Y and Salomon C 1996 *Phys. Rev. Lett.* **76** 4508
[59] Peik E, Ben Dahan M, Bouchoule I, Castin Y and Salomon C 1997 *Phys. Rev.* A **55** 2989
[60] Cladé P, de Mirandes E, Cadoret M, Guellati-Khelifa S, Schwob C, Nez F, Julien L and Biraben F 2006 *Phys. Rev.* A **74** 052109
[61] Sugarbaker A, Dickerson S M, Hogan J M, Johnson D M S and Kasevich M A 2013 *Phys. Rev. Lett.* **111** 113002
[62] Abend S *et al* 2016 *Phys. Rev. Lett.* **117** 203003
[63] Debs J E, Altin P A, Barter T H, Döring D, Dennis G R, McDonald G, Anderson R P, Close J D and Robins N P 2011 *Phys. Rev.* A **84** 033610
[64] Dickerson S M, Hogan J M, Sugarbaker A, Johnson D M S and Kasevich M A 2013 *Phys. Rev. Lett.* **111** 083001
[65] Hogan J M, Johnson D M S and Kasevich M A 2008 Light-pulse atom interferometry *Atom Optics and Space Physics: Proceedings of the International School of Physics* ed E Arimondo, W Ertmer, E M Rasel and W P Schleich (Amsterdam: IOS Press)
[66] Bongs K, Launay R and Kasevich M 2006 *Appl. Phys.* B **84** 599
[67] Louchet-Chauvet A, Farah T, Bodart Q, Clairon A, Landragin A, Merlet S and Pereira Dos Santos F 2011 *New J. Phys.* **13** 065025
[68] Tackmann G, Berg P, Schubert C, Abend S, Gilowski M, Ertmer W and Rasel E M 2012 *New J. Phys.* **14** 015002
[69] Guéry-Odelin D 2002 *Phys. Rev.* A **66** 033613
[70] Pedri P, Guéry-Odelin D and Stringari S 2003 *Phys. Rev.* A **68** 043608
[71] Pethick C J and Smith H 2001 *Bose–Einstein Condensation in Dilute Gases* (Cambridge: Cambridge University Press)
[72] Castin Y and Dum R 1996 *Phys. Rev. Lett.* **77** 5315
[73] Kagan Y, Surkov E and Shlyapnikov G 1996 *Phys. Rev.* A **54** R1753
[74] Huang K 1987 *Statistical Mechanics* (New York: Wiley)
[75] Shvarchuck I, Buggle C, Petrov D S, Kemmann M, von Klitzing W, Shlyapnikov G V and Walraven J T M 2003 *Phys. Rev.* A **68** 063603
[76] Giorgini S, Pitaevskii L P and Stringari S 2008 *Rev. Mod. Phys.* **80** 1215
[77] Ketterle W and Zwierlein M W 2008 Ultracold Fermi gases *Proc. Int. School of Physics 'Enrico Fermi' Course CLXIV* p 95
[78] Lassablière L and Quéméner G 2018 *Phys. Rev. Lett.* **121** 163402
[79] Condon G, Fortun A, Billy J and Guéry-Odelin D 2014 *Phys. Rev.* A **90** 063616
[80] Corgier R, Amri S, Herr W, Ahlers H, Rudolph J, Guéry-Odelin D, Rasel E M, Charron E and Gaaloul N 2018 *New J. Phys.* **20** 055002
[81] Rudolph J *et al* 2015 *New J. Phys.* **17** 065001
[82] Becker D *et al* 2018 *Nature* **562** 391
[83] van Zoest T *et al* 2010 *Science* **328** 1540
[84] Varoquaux G, Nyman R A, Geiger R, Cheinet P, Landragin A and Bouyer P 2009 *New J. Phys.* **11** 113010
[85] Elliott E R, Krutzik M C, Williams J R, Thompson R J and Aveline D C 2018 *NPJ Microgravity* **4** 16
[86] Gibney E 2018 *Nature* **557** 151